NURETH14-402

A SIMULTANEOUS OBSERVATION OF BUBBLE GROWTH AND MICROLAYER BEHAVIOR FOR AN ISOLATED BOILING REGIME OF SATURATED WATER

In-Cheol Chu¹, Hee Cheon NO² and Chul-Hwa Song¹

¹ Korea Atomic Energy Research Institute, Daejeon, Korea ² Korea Advanced Institute of Science and Technology, Daejeon, Korea

Abstract

The bubble growth rate and microlayer behavior were simultaneously visualized for an isolated boiling regime of saturated water. The increase rate of the bubble volume dropped sharply when the microlayer was totally depleted. However, the contribution of the superheated liquid layer evaporation to the bubble volume increase was comparable to or even higher than that of the microlayer evaporation during the time when the microlayer evaporation was active. The microlayer under the coalesced bubble was much thicker than that under single isolated bubble.

Introduction

Owing to the high efficiency of the boiling heat transfer, a lot of works have been continuously carried out in order to identify the heat transfer mechanism related with a bubble growth. Sharp [1] was the first who found out the direct evidence of the existence of the microlayer beneath the growing bubble. Using an interferometry technique, he observed the formation, evaporation, and dryout of a thin film of liquid beneath the growing bubble on a heated surface. Cooper and Lloyd [2] provided further evidence of the existence of the microlayer. They measured the instantaneous variation of the surface temperature at a number of locations beneath the bubbles, computed the spatial distribution of surface heat flux, and deduced the thickness of the microlayer. Also, Cooper [3] presented a theory that predicted the bubble growth rate in saturated boiling systems that involved the microlayer evaporation phenomena. Jawurek [4] measured the shape and the thickness of the microlayer, and the bubble growth for methanol and ethanol, using an optical interferometric technique and high-speed photography.

Zhao et al. [5] proposed a new dynamic microlayer model to predict the heat flux in fully developed nucleate boiling regions including critical heat flux. In their model, the boiling heat transfer was mainly attributed to the evaporation of the microlayer. Das et al. [6] developed an analytical model of boiling heat transfer based on the evaporation of the microlayer and the superheated liquid layer (macrolayer) around the bubble periphery, considering the temporal and spatial variations of the temperature in the liquid layer. However, it is still challenging to predict the contribution of the evaporations from the microlayer and the macrolayer on the bubble growth.

In the present study, the behaviors of bubble growth, coalescence, and the microlayer were simultaneously visualized for an isolated boiling regime, using a side view, a diagonal view, and a total reflection technique, respectively.

1. Experimental apparatus and visualization method

The present experimental facility consists of a boiling pool with a transparent heating surface, a power supply system, a data acquisition and control system, a lighting system, and two high speed video cameras. The boiling pool had a cubic shape. The side walls and top plate were made of a transparent polycarbonate plate, and the bottom plate was made of an aluminum plate. A reflux condenser was installed on the top plate of the boiling. The top of the reflux condenser was open to the ambient. As a result, the pressure of the boiling pool was maintained at an atmospheric pressure. Two auxiliary cartridge heaters were inserted through the side wall to control the pool temperature and maintain the pool at a saturated condition. The pool temperature was monitored by a few thermocouples. Special grade type-K thermocouples, manufactured by Watlow Inc., were used. The sheath diameter of the thermocouples was 0.5 mm. The thermocouples were located close to the boiling region of the transparent heating surface, but not inside the boiling region.

A rectangular sapphire substrate was sit at the central part of the bottom plate. The area and thickness of the sapphire substrate were $80 \times 120 \text{ mm}^2$ and 1 mm, respectively. The sapphire substrate was 15 mm higher than the top surface of the bottom plate in order to provide clear visualization path for the side view experiments. An ITO (Indium Tin Oxide) layer was used as a heating source because it was not only electro-conductive but also transparent. A 350 nm thick ITO layer was sputtered at the bottom surface of the sapphire substrate. The area of the ITO layer was $8 \times 100 \text{ mm}^2$. The sheet resistance of the ITO layer was approximately 10 Ohm/Sq., and the light transmission rate of the ITO layer was approximately 80% in the visible spectrum. The sapphire substrate sputtered with the ITO was supplied by Diamond Coatings Ltd. Silver electrodes having an area of $8 \times 10 \text{ mm}^2$ were printed on both ends of the ITO layer by Diamond Coatings Ltd. As a result, the heating area of the ITO layer became $8 \times 80 \text{ mm}^2$. In case of the diagonal view test, the width of the ITO layer was reduced to 2.7 mm.

Two identical high speed video (HSV) cameras were used. The HSV cameras are Memrecam GX-3 (color) manufactured by NAC Inc. One was for the total reflection. The other was installed in front of the boiling pool in order to observe the boiling structure in a lateral direction and/or a diagonal direction. In case of the diagonal view observation, the HSV camera and Xenon HID lamp were aligned to have an inclination angle of approximately 39° from the horizon following the suggestion of Bang et al. [13]. A Xenon HID lamp was installed at the opposite side of the boiling pool. MICRO NIKKOR 105 mm 1:2.8 lens was installed to each camera. Well synchronized boiling images were obtained from two HSV cameras by providing an external TTL signal from the data acquisition and control unit.

Refraction of light bends the light ray toward the tangent to the boundary between the two media when it pass from higher refractive index (n_1) medium to lower refractive index (n_2) medium. The refraction is described by Snell's law which states that no light can pass through and all of the light is reflected back above a certain angle (so called 'critical angle'). This phenomenon is the total internal reflection.

The optical setup for the present total reflection is schematically illustrated in Fig. 1. A laser beam was incident on the sapphire substrate via the prism block. A prism shaped pyrex block was attached to the ITO layer underneath the sapphire substrate to match the incident angle for

the total reflection at the top surface of the sapphire substrate. Silicon oil layer was filled between the top of the prism block and the bottom of the sapphire substrate in order to completely remove the gas phase between them. Otherwise, the total reflection would occur on the top surface of the prism block where gas phase exists. Ion laser with the wavelength of 488 and 514.5 nm was used as a light source for the total reflection. The laser is Spectra-Physics Model 177G, having 300 mW power and beam diameter of 0.82 mm. A spatial filter was installed in front of the laser system to remove random fluctuations from the intensity profile of the laser beam. The spatial filter consists of an objective lens ($60 \times$) and a pinhole (diameter of 15 µm). Laser beam diameter expanded approximately to 20-25 mm after it pass through the collimator lens (diameter of 2") located behind the pinhole. Two mirrors were used to control the incidence angle of the laser beam and the collection angle of the total reflection beam. A laser line filter was installed in front of the total reflection camera when the total reflection was synchronized with the side view or diagonal view observations. The laser line filter, having a center wavelength of 488 \pm 2 nm and FWHM (full width half maximum) wavelength of 10 \pm 2 nm, effectively eliminate the randomly reflected light.

The laser beam incident on the prism block was inclined approximately 45° from the horizon in the present experiments. The incident angle was higher than the critical angle at which the total reflection occurs when the top surface of the sapphire was occupied with gas phase. But, the incident angle became lower than the critical angle of the total reflection when the top surface of the sapphire was wetted by liquid. As a result, for nucleate boiling condition, the region where liquid is dried out appears bright in the total reflection image, and the region wetted by liquid appears dark.

The images for the analysis of single bubble growth and the contribution of microlayer evaporation were recorded at the frame rate of 20,000 fps. The spatial resolutions of these images were (1) 28 μ m (width) and 40 μ m (height) per pixel for the total reflection, and (2) 33 μ m (width and height) per pixel for the side view. The images to observe the inside and/or the underneath structure of the coalescing bubbles were obtained at the frame rate of 5,000 fps. The spatial resolutions of these images were (1) 32 μ m (width) and 46 μ m (height) per pixel for the total reflection, and (2) 32 μ m (width) and 73 μ m (height) per pixel for the diagonal view. The shutter speed was increased to 197 μ sec for the diagonal observation, but the shutter speed did not exceed 10 μ sec in the side view and the total reflection observations.

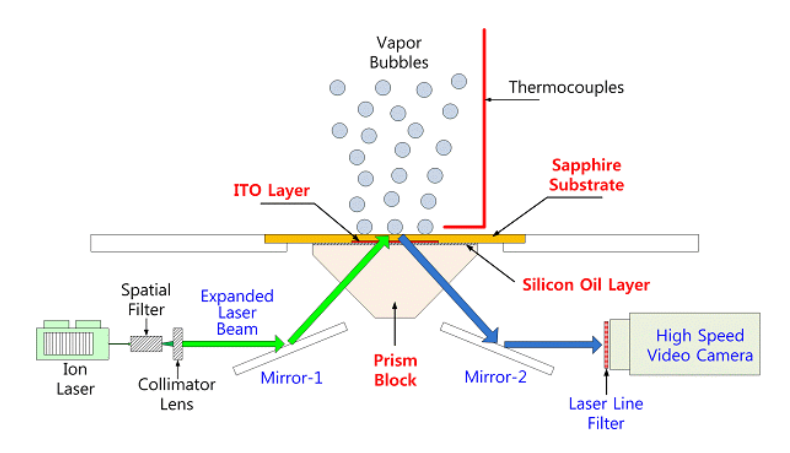


Fig. 1 Schematic of the test apparatus

2. Experimental results and discussion

2.1 Bubble growth rate and the contribution of microlayer evaporation

Figure 2 shows the consecutive images of isolated bubbles from the time of nucleation to the time of departure in the horizontal pool boiling of saturated water. The pictures were taken by the synchronized side view and total reflection observations at the heat flux of 45 kW/m² (5% CHF). The heat flux was calculated by dividing the heat production rate by the area of ITO layer without considering the heat loss to the ambient. The measured critical heat flux was 907 kW/m². The size of the side view images are 5.7×4.9 mm (width × height), and 5.7×5.7 mm (width × height) for the total reflection. The bubble behaviors are presented with a time step of 0.25 msec or 0.5 msec.

Typically, two zones appear in the total reflection images for an early bubble growth period (*e.g.*, from 1.0 – 4.25 msec for the right side bubble). One is a circle in the center, and the other is an annulus around the circle. The total reflection can occur at the shallow liquid layer having a smooth gas interface as well as at the dried boiling surface. Therefore, two kinds of total reflections are expected to occur at the base of bubble. One is from the central dry spot, and the other is from the interface between the microlayer and the bubble base, as illustrated in Fig. 3. The previous works also reported that the interface between the microlayer and the bubble base is slightly inclined [4], which causes the reflection angle from the microlayer to be different with the reflection angle from the dry spot. Unless the curvature of the microlayer at the triple point is sufficiently huge, there exists a discontinuity in the total reflection light at this triple point, as illustrated in Fig. 4. In conclusion, the dark ring in the total reflection images in Fig. 2 corresponds to the boundary between the dry spot and the microlayer. In addition, as illustrated in Fig. 5, the central bright area does not appear when the dry spot area is negligibly small, as in the total reflection image at 0.25 msec. The spatial resolution of the total reflection image mentioned above would be the minimum detectable size of the dry spot.

At the very beginning stage of the bubble growth, the bubble expands much rapidly due to the high inertia of the pressure potential built inside the bubble (Rayleigh [7]; Robinson and Judd [8]). This period is generally termed the *inertia controlled growth stage*. When the pressure inside the bubble is balanced with the pressure outside the bubble, the bubble growth is governed by the rate at which energy is transferred to the bubble through the bubble-liquid interface (Plesset and Zwick [9]; Forster and Zuber [10]; Mikic *et al.* [11], Robinson and Judd [8]). This is generally termed the *diffusion or heat transfer controlled growth stage*. However, it is not well defined and/or evaluated when the inertia controlled growth stage transits to the diffusion controlled stage, and how much energy is transferred to the bubble by each mechanism during the transition period between two stages. Kim *et al.* (2005) measured the bubble growth rate in a horizontal pool of saturated freon R-113 at the atmospheric pressure. The temperature of the boiling surface was controlled to be constant at 72 °C. They reported that the inertia controlled stage ends at about 1.0 – 1.2 msec in their experimental condition.

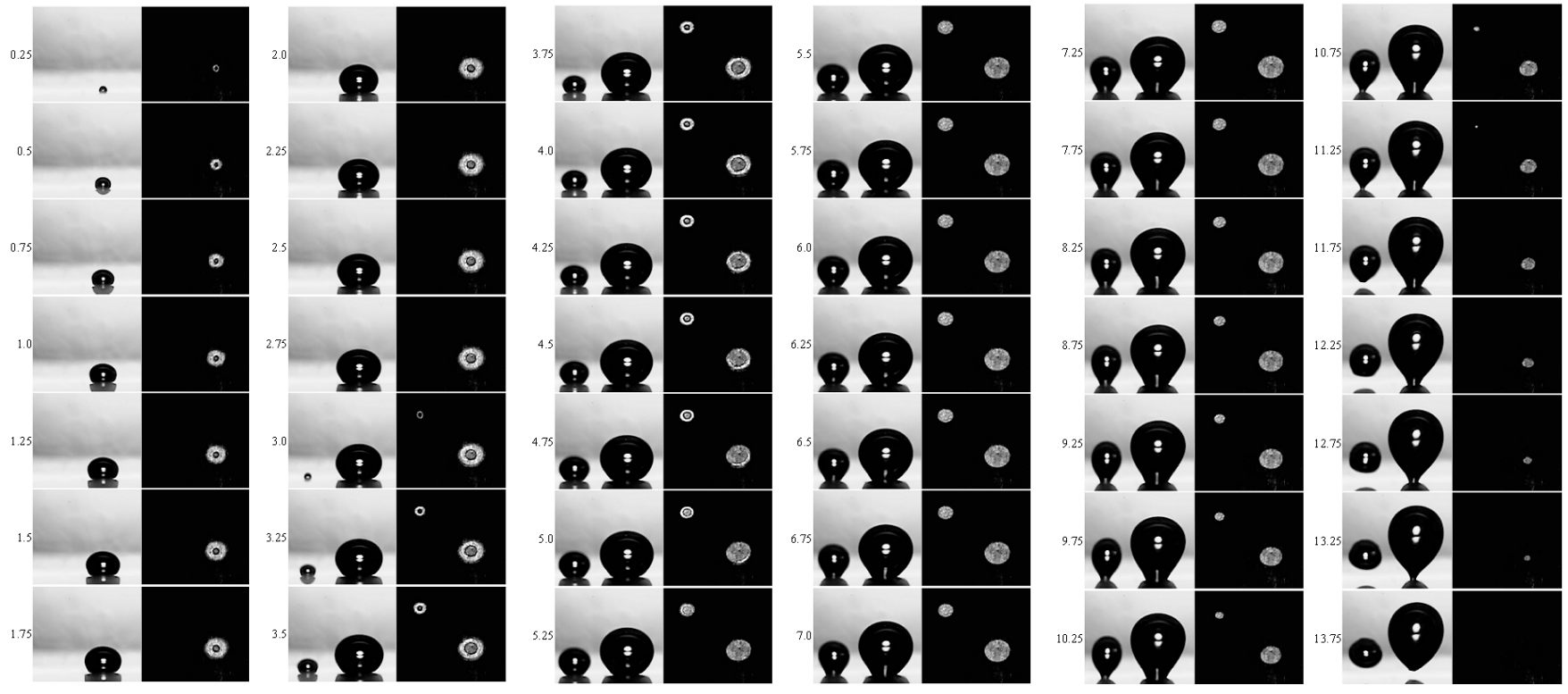


Fig. 2 Consecutive images of the synchronized side view (SV) and total reflection (TR). Time is msec.

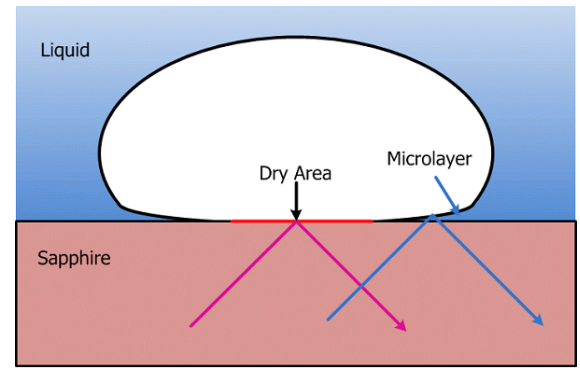


Fig. 3 Total reflection from a bubble

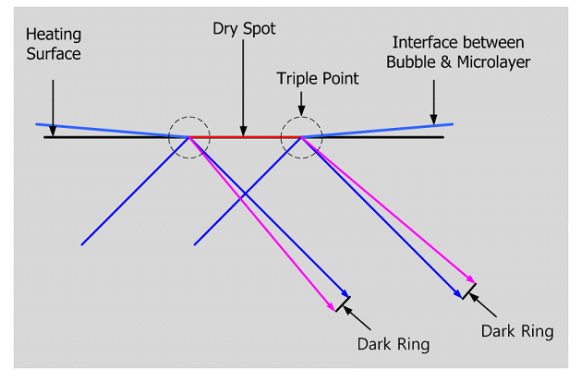


Fig. 4 Total reflection at the triple point

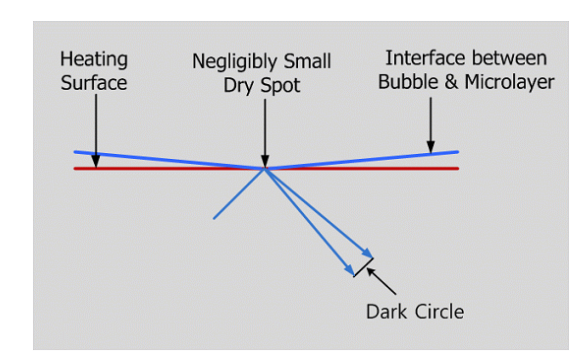


Fig. 5 Total reflection at the initial bubble growth period

In the present total reflection images of the bubble growth in Fig. 2, the dry spot is much smaller than the microlayer area up to the time of 1.0 msec. Especially, the dry spot is undetectable at 0.25 msec. This supports the fact that the bubble growth at this period is governed by the momentum interaction between the bubble and the liquid pool (inertia controlled growth stage), not by the heat transsfer through the bubble interface. We also can see, from the side view and total reflection images up to the time of 0.5 msec, that the establishment of the microlayer precedes the formation of the dry spot, explaining that the bubble growth by the inertia of the pressure potential overwhelms the bubble growth by the evaporation of the microlayer. In the diffusion controlled bubble growth period, the bubble grows by the evaporation of the microlayer (q_{micro}^*) underneath the bubble and the evaporation of the superheated liquid layer (q_{SLL}^*) around the bubble periphery, as illustrated in Fig. 3. The outer diameter of the microlayer increases with an expansion of the bubble base due to the evaporation of the microlayer and the superheated liquid layer (hereafter, macrolayer). Also, the area of the dry spot increases as the inner part of the microlayer is depleted by the evaporation.

The changes of the equivalent bubble diameter and volume were evaluated from the side view images in Fig. 6, and the results are shown in Fig. 7. The bubble diameter was calculated from the bubble area projected to the side view camera, which was the sum of the total pixel area inside the bubble. The bubble diameter and volume increased more steeply until approximately 5.25 msec. This corresponded to the time of the total depletion of the microlayer as can be seen in the total reflection images in Fig. 2. After the total depletion of the microlayer, the bubble grew only by the evaporation of the macrolayer.

Contribution of the microlayer evaporation and the macrolayer evaporation to the bubble growth is an interesting subject in predicting the boiling heat transfer phenomena. However, it is still challenging to predict the contribution of the evaporations from the microlayer and the macrolayer on the bubble growth. In the present study, the contributions of the microlayer and macrolayer evaporation, and the inertia pressure potential were roughly estimated for the bubble growth shown in Fig. 2.

The evaporation heat transfer rate from the macrolayer can be evaluated using the volume increase rate data after the total depletion of the microlayer. Then, the volume increase rate from the evaporation of the microlayer can be deduced by subtracting the volume increase rate due to the evaporation of the macrolayer from the total volume increase rate of the bubble.

The volume increase rate of the bubble is equivalent to the energy transfer rate through the bubble interface by the evaporation of the microlayer and the macrolayer. As shown in Fig. 8, the volume increase rate reached the maximum at approximately 3.25 - 3.5 msec. This was the time when the bubble base length and the microlayer area were close to the maximum values, thus producing the maximum evaporation heat transfer rate. However, the volume increase rate dropped sharply at around 5.0 msec at which the microlayer was almost evaporated out. Thereafter, the volume increase rate decreased mildly until the bubble departed from the heated surface, corresponding mainly to the continuous decrease of the perimeter of the bubble base, i.e., the heat transfer area of the macrolayer.

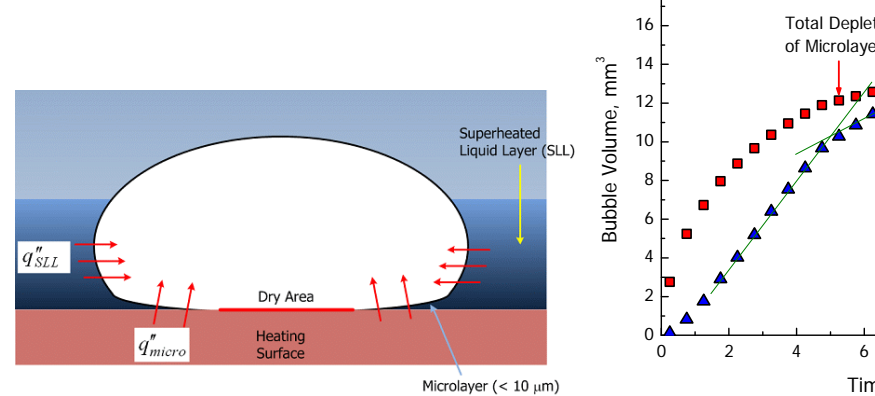


Fig. 6 Evaporation of micro- & macro-layers

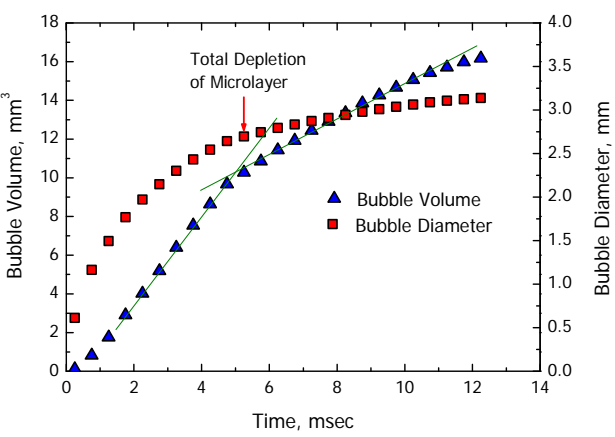


Fig. 7 Bubble growth in diameter & volume

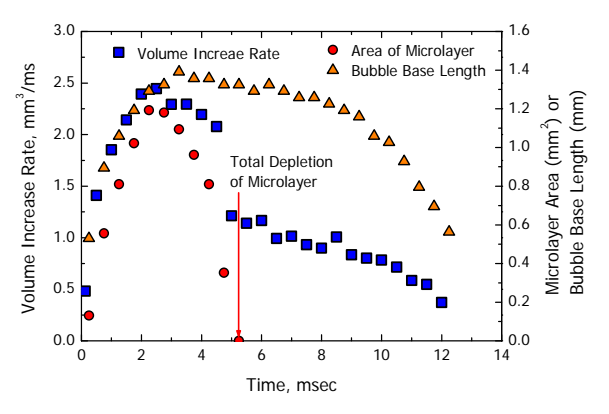


Fig. 8 Bubble volume increase rate versus the microlayer area and bubble base length

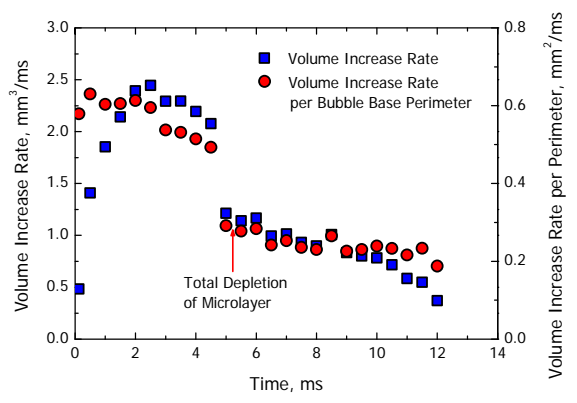


Fig. 9 Volume increase rate per bubble base perimeter

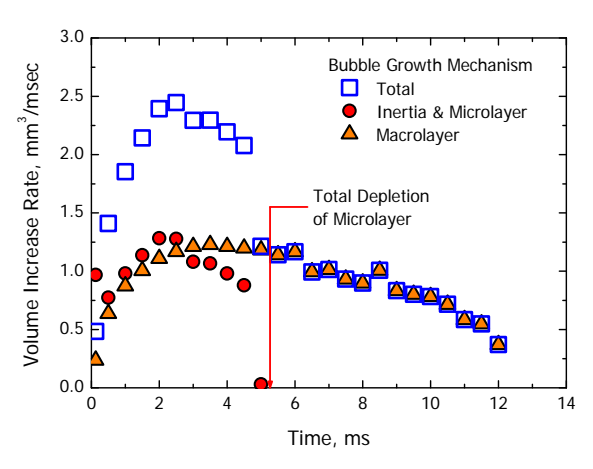


Fig. 10 Partition of bubble growth rate

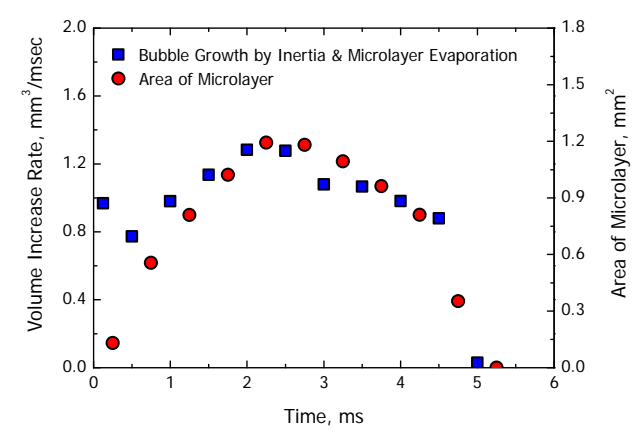


Fig. 11 Bubble growth rate by inertia and microlayer evaporation versus microlayer area

The bubble growth rate and the growth rate per bubble base perimeter are also shown in Fig. 9. The steep increase of the volume increase rate of the bubble at the period of 0.1 - 1.35 msec was attributed to the increase of the bubble base perimeter, meaning the increase of the interfacial area for the microlayer and macrolayer evaporations. Comparing the bubble shape at the time of 5.5 msec and 11.5 msec, the bubble at 5.25 msec has higher interfacial area for the macrolayer evaporation per the bubble base perimeter than the bubble at 11.5 msec. Therefore, the volume increase rate per perimeter at 5.5 msec was higher than that at 11.5 msec (Fig. 9). It is possible to deduce the bubble volume increase rate due to the macrolayer evaporation for the period 0.25 – 5.25 msec by considering the volume increase rate per bubble base perimeter after 5.25 msec. The volume increase rate per bubble base perimeter at the period of 5.5 - 5.75 msec was roughly assumed to be equal to the volume increase rate per perimeter by the macrolayer evaporation at the period of 0.25 - 5.0. It was because that the bubble base shape at the period of 5.5 - 5.75msec was similar to that at the period of 0.25 - 5.0. The volume increase rate of the bubble by the macrolayer evaporation from the nucleation to the departure was quantified based on the above assumption (Fig. 10). In addition, the volume increase rate of the bubble by the inertia and the microlayer evaporation was evaluated by subtracting the volume increase rate due to the macrolayer evaporation from the total volume increase rate (Fig. 10). The contribution of the macrolayer evaporation to the bubble volume increase was comparable to or even higher than that of the microlayer evaporation during the time of 0.75 - 4.75 msec when the microlayer evaporation was active (Fig. 10). The total contribution the macrolayer evaporation to the whole process of the bubble growth was estimated to be about 70%, and the rest of the bubble growth was due to the inertia controlled growth and the microlayer evaporation.

The bubble growth due to the microlayer evaporation was closely related to the projected area of the microlyaer underneath the bubble and the bubble volume increase rate due to the microlayer evaporation showed the same tendency with the area of the microlyaer (Fig. 11). However, at the time of 0.25 msec, the bubble volume increase rate was about 75% of the maximum bubble volume increase rate even though the area of the microlayer was about 10% of the maximum area. This discrepancy was due to the bubble growth driven by the inertia.

2.2 Thick microlayer underneath the coalesced bubble

To observe the behavior of the dry spot and the microlayer, the diagonal view technique was simultaneously applied with the total reflection technique. Generally, the initial bubble growing motion was not sufficiently definite in the diagonal images because the shutter speed was low to $197 \mu sec$. But, it did not hinder the clear understanding on the behavior of the dry spot and the microlayer.

Figure 12 shows the coalescence process of two bubbles at the heat flux of 500 kW/m² (37.2% CHF). The measured critical heat flux was 1,345 kW/m². The increase in the critical heat flux was probably due to the fact that the width of the boiling surface was narrowed to 2.7 mm. The heat generated by the ITO is delivered to the boiling surface by two-dimensional conduction heat transfer, therefore some of the heat diffuses to the non-heating region. The fraction of heat diffusion increases with the decrease of ITO width. As a result, higher heat production rate is required for a narrow ITO to achieve the same heat flux on the boiling surface.

For the bubble in the right side, the total reflection from the left side of the microlayer disappears at 2.0 msec. This implies that the left side microlayer of the bubble in the right side experiences some disturbance. As will be clearly seen in Fig. 13, the microlayer is agitated by the growth of the bubble in the left side. Two bubbles collide with each other at 4.0 msec, and start to coalesce at 6.0 msec. After the coalescence of bubbles, two primary dry spots co-exist underneath the coalesced bubble. Throughout the evaporation of the liquid layer under the bubble, two primary dry spots expand and they come closer to each other as time goes by. But, the merge of these dry spots does not occur until the departure of the bubble possibly because the expansion speed of the dry spots is not sufficient due to the relatively low heat flux.

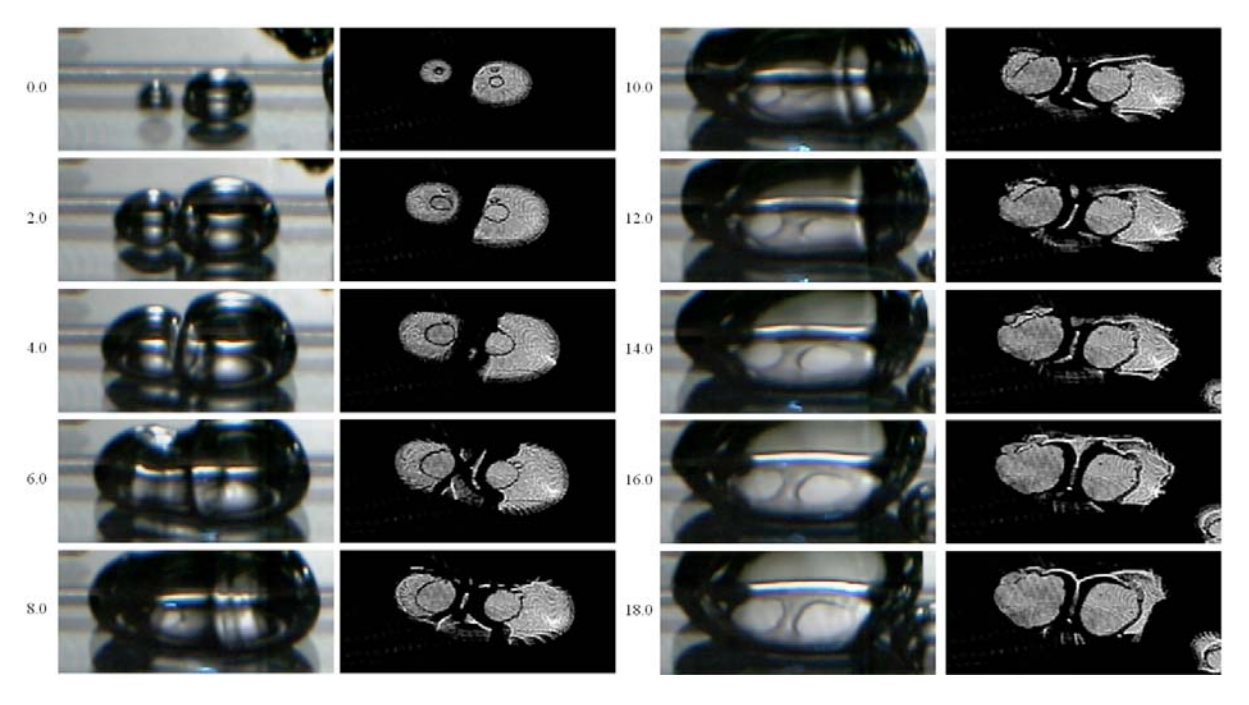


Fig. 12 Consecutive images of the diagonal view and total reflection, showing the bubble coalescence process. Time is msec.

An interesting phenomenon of the bubble coalescence is that the microlayer is not as thin as the microlayer under a single isolated bubble. Figure 13 clearly shows why the microlayer becomes thicker when bubbles coalesce. The images were obtained at the heat flux of 903 kW/m2 (67.1% CHF). Coalescence of multiple bubbles is more common than the coalescence of two bubbles at this heat flux level. Similar and/or almost identical images explaining the thickening mechanism of the microlayer were obtained at lower heat flux conditions, but the images in Fig. 13 captured the phenomena in the best way. At time 0.0 msec, the bubble in the left already passed the rapid growth period and the bubble in the right is in its early stage of growth. The bubble in the right grows so fast that they contact with each other within 1.0 msec. The liquid around the bubble is pushed more strongly away from the bubble as the bubble grows more rapidly. The pushed liquid by the bubble in the right penetrates deep into the microlayer of the bubble in the left bubble. The surge of the liquid into the microlayer of the left bubble is clearly shown at the diagonal images at 1.0, 1.6, and 2.2 msec in Fig. 13. The penetration ceases when the inertia

force balances with the drag force. At the same time, the total reflection from this agitated thick microlayer disappeared.

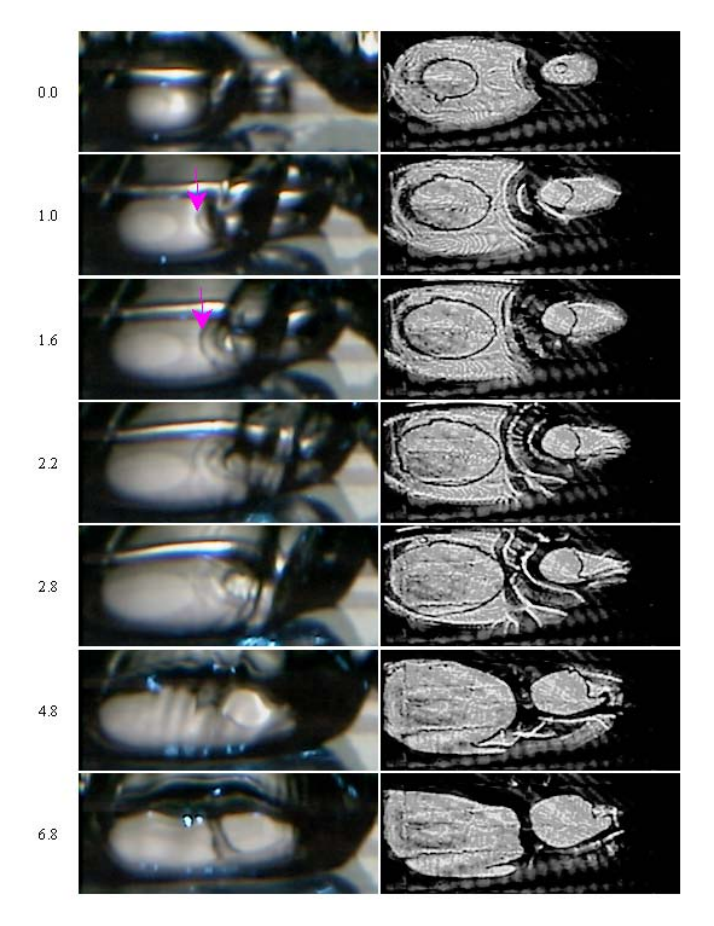


Fig. 13 Consecutive images of the diagonal view and total reflection, showing the microlayer thicknening phenomenon. Time is msec.

3. Conclusions

The bubble growing mechanisms were analyzed by the synchronized observations of the lateral view and the total reflection for an isolated bubble in a saturated horizontal water pool boiling. The volume increase rate of the bubble and the projected area of the microlayer were quantified from the synchronized observations. In the present experimental condition, the total contribution of the macrolayer evaporation to the whole bubble growth process dominated over the contributions of the inertia and the microlayer evaporation. The bubble growth due to the microlayer evaporation was closely related to the area of the microlayer underneath the bubble. However, a precise estimation of the temperature field is necessary for more accurate evaluation of the bubble growth mechanisms of the macrolayer and microlayer evaporations and the inertia driven growth.

Bubble coalescence occurs very frequently from the intermediate heat flux conditions. The microlayer under the coalesced bubble was much thicker than that under single isolated bubble because the liquid around the bubble is pushed away from the bubble as the bubble grows

rapidly. Therefore, we should consider the difference in the evaporation heat transfer of this much thicker microlayer when we intend to analyze the boiling heat transfer in a microscopic way.

4. References

- [1] R. R. Sharp, "The Nature of Liquid Film Evaporation during Nucleate Boiling", <u>NASA TN D-1997</u>, 1964.
- [2] M. G. Cooper and A. J. P. Lloyd, "The Microlayer in Nucleate Pool Boiling", Int. J. Heat Mass Transfer, Vol. 12, 1969, pp. 895-913.
- [3] M. G. Cooper, "The Microlayer and Bubble Growth in Nucleate Pool Boiling", Int. J. Heat Mass Transfer, Vol. 12, 1969, pp. 915-933.
- [4] H. H. Jawurek, "Simultaneous Determination of Microlayer Geometry and Bubble Growth in Nucleate Boiling", Int. J. Heat Mass Transfer, Vol. 12, 1969, pp. 843-848.
- [5] Y.-H. Zhao, T. Masuoka, and T. Tsuruta, "Unified Theoretical Prediction of Fully Developed Nucleate Boiling and Critical Heat Flux Based on a Dynamic Microlayer Model", Int. J. Heat Mass Transfer, Vol. 45, 2002, pp. 3189-3197.
- [6] A. K. Das, P. K. Das, and P. Saha, "Heat Transfer during Pool Boiling Based on Evaporation from Micro and Macrolayer", Int. J. Heat Mass Transfer, Vol. 49, 2006, pp. 3487-3499.
- [7] J. W. S. Rayleigh, "On the Pressure Developed in a Liquid during the Collapse of a Spherical Cavity", Phil. Mag., Vol. 34, 1917, pp. 94-98.
- [8] A. J. Robinson and R. L. Judd, "Bubble Growth in a Uniform and Spatially Distributed Temperature Field", Int. J. Heat Mass Transfer, Vol. 44, 2002, pp. 2699-2710.
- [9] M. S. Plesset and S. A. Zwick, "The Growth of Vapor Bubble in Superheated Liquid", J. Appl. Phys., Vol. 25, 1954, 493-500.
- [10] H. K. Foster and N. Zuber, "Growth of Vapor Bubbles in Superheated Liquid", J. Appl. Phys., Vol. 25, 1954, 474-478.
- [11] B. B. Mikic, W. M. Rohsenow and P. Griffith, "On Bubble Growth Rates", Int. J. Heat Mass Transfer, Vol. 13, 1970, pp. 657-665.
- [12] J. Kim, J. Lee and M. H. Kim, "Experimental Study on Single Bubble Growth under Subcooled, Saturated, and Superheated Nucleate Pool Boiling", J. Mech. Sci. Technol., Vol. 20, 2006, pp. 692-709.
- [13] I. C. Bang, S. H. Chang and W.-P. Baek, "Visualization of a Principle Mechanism of Critical Heat Flux in Pool Boiling", Int. J. Heat Mass Transfer, Vol. 48, 2005, pp. 5371-5385.